Effects of build orientation and element partitioning on microstructure and mechanical properties of biomedical Ti-6Al-4V alloy produced by laser sintering

Effects of build orientation and element partitioning on microstructure and mechanical properties of biomedical Ti-6Al-4V alloy produced by laser sintering

P. Mengucci[1]*, A. Gatto[2], E. Bassoli[2], L. Denti[2], F. Fiori[3], E. Girardin[3], P. Bastianoni[1], B. Rutkowski[4], A. Czyrska-Filemonowicz[4], G. Barucca[1]

[1] Dipartimento SIMAU, Università Politecnica delle Marche, 60131 Ancona, Italy.

[2] Dipartimento DIEF, Università di Modena e Reggio Emilia, Via Vivarelli 10, 41125 Modena, Italy.

[3] Dipartimento DISCO, Università Politecnica delle Marche, 60131 Ancona, Italy.

[4] International Centre of Electron Microscopy for Material Science & Faculty of Metals Engineering and Industrial Computer Science, AGH University of Science and Technology, Al. A. Mickiewicza 30, 30-059 Kraków, Poland.

*** Corresponding author:**

Paolo Mengucci
Dip. SIMAU, Università Politecnica delle Marche
I-60131 Ancona
Italy
E-mail: p.mengucci@univpm.it

Abstract

Direct Metal Laser Sintering (DMLS) technology was used to produce tensile and flexural samples based on the Ti-6Al-4V biomedical composition. Tensile samples were produced in three different orientations in order to investigate the effect of building direction on the mechanical behavior. On the other hand, flexural samples were submitted to thermal treatments to simulate the firing cycle commonly used to veneer metallic devices with ceramics in dental applications. Roughness and hardness measurements as well as tensile and flexural mechanical tests were performed to study the mechanical response of the alloy while X-ray diffraction (XRD), electron microscopy (SEM, TEM, STEM) techniques and microanalysis (EDX) were used to investigate sample microstructure. Results evidenced a difference in the mechanical response of tensile samples built in orthogonal directions. In terms of microstructure, samples not submitted to the firing cycle show a single phase acicular α' (hcp) structure typical of metal parts subject to high cooling rates. After the firing cycle, samples show a reduction of hardness and strength due to the formation of laths of the β (bcc) phase at the boundaries of the primary formed α' plates as well as to lattice parameters variation of the hcp phase. Element partitioning during the firing cycle gives rise to high concentration of V atoms (up to 20 wt%) at the plate boundaries where the β phase preferentially forms.

Keywords: Ti alloys; laser sintering; heat treatments; mechanical properties; structure characterization; element partitioning

1. Introduction

Among Ti alloys, the Ti-6Al-4V composition is one of the most used in industrial applications ranging from aerospace to power generation, from automotive to biomaterials [Polmear, 2006; Lutjering and Williams, 2007]. Low weight, high specific strength, excellent fatigue and corrosion resistance are the basic properties fostering applications. The wide interest addressed to the Ti-6Al-4V composition is due to the possibility of the α+β systems, to which that composition belongs, to exhibit mechanical properties highly dependent on microstructure, which can be controlled by thermal and thermo-mechanical treatments [Ahmed et al., 1998; Zeng et al., 2005; Matsumoto et al., 2016]. Fully lamellar, fully equiaxed and bi-modal (duplex) microstructures are commonly obtained in the α+β systems by changing the thermo-mechanical route processing [Lutjering and Williams, 2007]. Furthermore, submicrocrystalline (SMC) materials with improved mechanical properties can be obtained by severe plastic deformation routes associated to thermal treatments [Valiev et al., 2002; Zherebtsov et al., 2005].

Direct metal laser sintering (DMLS, Power Bed Fusion according to ASTM F42 committee) is an additive manufacturing (AM) technology, which offers a number of advantages with respect to conventional manufacturing techniques, such as net shape production, lower time to market, efficient use of materials, direct production based on a CAD model, high level of flexibility, cost savings [Shamsaeia et al., 2015; Song et al., 2012; Thijs et al., 2010]. Moreover, due to the additive process, DMLS is capable of producing complex geometrical features and low volume devices in a single production process. These latter capabilities are particularly useful for prosthetic applications in orthopedics and dentistry where a high degree of individualization is required.

However, the DMLS process undergoes several intrinsic problems such as high temperature gradients and high cooling rates that give rise to thermal stresses, segregation phenomena and development of non-equilibrium phases. Therefore, microstructural anisotropies leading to build orientation effects can be developed during the DMLS process [Wauthle et al., 2015]. In the same way, effects of build orientation on the mechanical properties of alloys produced by electron beam

melting were reported [Antonisamy et al., 2013]. In order to reduce the building anisotropies developed during the production processes, thermo-mechanical treatments, which can further affect the mechanical behavior of the alloy, are commonly adopted [Thijs et al., 2010, 2013; Vrancken et al., 2012].

Because of its broad applications in industry, the Ti-6Al-4V composition has received prime attention as a candidate for DMLS technology. Thermal and thermo-mechanical treatments performed to reduce the building orientation effects as well as to improve the mechanical properties of the Ti-6Al-4V composition have been largely adopted [Wauthle et al., 2015; Thjis et al., 2013; Vrancken et al., 2012; Wu et al., 2016; Ahmed et al., 2016]. In general, each treatment aims to control the $\alpha \leftrightarrow \beta$ transformations in order to attain specific morphology, size and texture of the constituent phases. Xu et al. (2015) have demonstrated the feasibility of in situ treatments capable of producing strong and ductile Ti-6Al-4V alloys while Barriobero-Vila et al. (2015) have discussed the role of element partitioning in the $\alpha \leftrightarrow \beta$ transformations and the influence of the lattice structure on the mechanical properties.

In this study, a Ti-6Al-4V alloy for biomedical applications has been produced by the DMLS technology in order to investigate the effects of building orientation and post-production treatments on the mechanical behavior of the alloy. A firing cycle consisting of five heating and cooling steps was adopted to simulate the veneering of metal parts with ceramics. Results obtained from tensile and flexural tests are discussed in function of the structural properties investigated by various microscopy techniques and X ray diffraction (XRD) method. In particular, the peculiar microstructure developed during the firing cycle, responsible of changes in mechanical behavior, was mainly correlated to element partitioning that produces laths of β phase highly enriched in V atoms at the boundaries of α plates and changes in lattice structure of the alloy.

2. Material and methods

2.1 Sintering parameters, material composition and properties

Starting from EOS Ti64 powder, supplied by EOS GmbH Electro Optical System, flexural and tensile specimens were produced by Direct Metal Laser Sintering (DMLS). The EOS Ti64 powder was virgin new, never used before for any previous laser sintering process.

An EOSINT M270 system equipped with a solid-state Yb fiber laser carried out the sintering process by using the laser sintering parameters reported in Table 1.

Table 1 about here

The material is Ti-6Al-4V alloy with chemical composition corresponding to ISO 5832-3, ASTM F1472 and ASTM B348. Nominal composition of the EOS Ti64 powder, as reported in the material datasheet provided by the manufacturer, is shown in Table 2.

Table 2 about here

In order to reduce anisotropies due to the layer-by-layer building method, heat treatment, consisting of ageing the as-sintered (AS) sample at 800 °C for 4 hours in argon inert atmosphere, was performed immediately after the laser production process. From now on, this thermal treatment is referred to as HT. Physical properties of the commercially available Ti64 alloy in the as-sintered (AS) and heat-treated (HT) state are listed in Table 3. Note that Ti64 alloy manufactured by EOS GmbH for biomedical applications is commercialized in the HT state, which will be treated as a reference one for the samples investigated in this study. All mechanical properties of investigated samples will be referred to values reported in Table 3 for the HT state. Mechanical properties in Table 3 are expressed as minimum values, which should be exceed to fulfill the minimum requirements of material specification standards ASTM F1472-08, ASTM B348-09 and ISO 5832-3:2000.

Table 3 about here

Material in the HT state shows a decrease of about 15% in strength and an increase of about 40% in elongation values with respect to the AS condition (Table 3), while Young modulus and hardness remain unaltered. These variations are caused by the HT treatment, performed directly after the production process.

2.2 Mechanical tests and firing cycle

Flexural specimens (FLEX) were produced according to ASTM B528-05 (Standard Test Method for Transverse Rupture Strength of Metal Powder Specimens) and B 925–08 (Standard Practices for Production and Preparation of Powder Metallurgy (PM) Test Specimens).

Tensile specimens (TENS) were built following ASTM E8M:11 (Standard Test Methods for Tension Testing of Metallic Materials).

Figure 1 shows geometry and dimensions of FLEX (Fig. 1a) and TENS (Fig. 1b) samples, respectively. In both drawings, Z is the direction of growth in the AM machine, and XY is the plane of powder deposition; X is the slide direction of the recoater. Dimensions in Figure 1 are in mm.

Figure 1 about here

In order to investigate possible variations of the mechanical properties with the sample building orientation, three different groups of tensile (TENS) specimens were produced. Each group consisted of 4 tensile samples. The different groups of samples were built with the axis of the tensile specimens oriented along three different directions of the building machine, as follows:

- TENS_0: axis parallel to the X direction;
- TENS_90: axis parallel to the Y direction;
- TENS_45: axis parallel to the bisector of the X-Y quadrant.

After additive fabrication, all samples belonging to both TENS and FLEX groups were submitted to the HT treatment. As already stated above, this represents the reference condition of our samples, which simulates the normal condition of commercialization of metallic devices obtained by additive manufacturing.

However, in dental applications, due to aesthetic reasons, metallic devices are often veneered with dental ceramic material during a firing operation carried out at high temperature. That thermal treatment, can induce modifications of microstructure and consequently cause changes of mechanical properties of the metallic devices. Therefore, in order to investigate also possible variations of mechanical properties and microstructure of the Ti-6Al-4V alloy due to the firing cycle (FC), a five-step thermal treatment was adopted in this work. Details of this standard five-step cycle, compliant to EN ISO 22674, are outlined in Figure 2. Starting from a pre-heating temperature of 420 °C, five steps simulate the firing of oxide and ceramic layers.

Figure 2 about here

In total, four samples of the FLEX group were submitted to the firing cycle (FC) described above. From now on, samples belonging to this thermally treated group are indicated as $FLEX_{FC}$.

Details of the mechanical tests performed on samples of the TENS, FLEX and $FLEX_{FC}$ groups are summarized in the following:

- Tensile tests (crosshead speed 5 mm/min, load cell capacity of 250 kN);
- Three point bending tests (support width 25.4 mm, crosshead speed 2 mm/min, load cell capacity of 30 kN).

2.3 Hardness measurements

Rockwell C hardness tests, based on ISO 4498:2010 (Sintered metal materials, excluding hard metals -- Determination of apparent hardness and microhardness), were performed by means of an

ERNST NR3D Hardness tester, following the specifications of ISO 6508-1:2015 (Metallic materials -- Rockwell hardness test).

2.4 Roughness measurements

Roughness measurements adhering to EN 10049:2013 were carried out by means of a DIAVITE DH-5 stylus tester, by adopting a travel length l_t of 4.8 mm, with a cut-off filter of 0.8 mm, giving an evaluation length l_m of 4 mm. Five measurements per sample were recorded for statistical reasons, taken on XZ faces along the X direction. The standard deviations (SD) associated to the roughness value were estimated from the five measurements.

2.5 Statistical tests

Statistical tests were performed in order to assess whether the heat treatments cause significant changes in the mechanical response. Possible significant differences between the groups were checked by means of the t-test for independent samples by using a software tool for statistical analysis (Statistica 8, Statsoft). The test can be used to determine if two sets of data are significantly different from each other. It results in probability values (p-values): when lower than 0.05 they can be taken as a decision to reject the null hypothesis of equality between two groups of samples.

2.6 Structure characterization

In order to correlate the mechanical behavior of samples to their microstructure, samples from the TENS, FLEX and $FLEX_{FC}$ groups were structurally characterized by the analytical techniques listed below. All samples submitted to structural characterization were not mechanically tested. Morphological and structural characterization of the EOS-Ti64 powder was also performed.

Structural characterizations were carried out by X-ray diffraction (XRD), scanning electron microscopy (SEM), transmission electron microscopy (TEM), scanning transmission electron microscopy (STEM) and energy dispersive X-ray microanalysis (EDX).

A Bruker D8 Advance diffractometer operating at V= 40 kV and I= 40 mA, with Cu-Kα radiation, in the angular range 2θ=10 - 80° was used for XRD measurements.

SEM observations were carried out by a Zeiss Supra 40 field emission scanning electron microscope (SEM) equipped with a Bruker Z200 EDX microanalysis.

A Philips CM200 and a JEOL JEM-2010 ARP equipped with an Oxford Inca energy dispersive X-ray microanalysis, both operating at 200 kV, were used for TEM observations.

Analytical high resolution microscopy as well as EDX analysis were carried out by a probe Cs-corrected FEI Titan^3 G2 60-300 equipped with ChemiSTEM technology (X-FEG field-emission gun and Super-X EDX detector system) developed at FEI (FEI application note AN002707-2010. Available from: www.fei.com).

TEM bright-field (TEM-BF) imaging and STEM imaging using high-angle annular-dark-field (HAADF) contrast as well as EDX mapping and high-resolution TEM (HRTEM) imaging were used for characterization of the samples micro/nanostructure and chemical composition of phases down to the nano-scale. Phase identification was performed by selected area electron diffraction (SAED), STEM-EDX and fast Fourier transform (FFT) of HR(S)TEM images. The diffraction patterns and HR(S)TEM images were interpreted with the JEMS software (Stadelman 2007).

Samples for TEM observations were mechanically prepared by grinding on abrasive papers and polishing on diamond pastes. Disks with a 3 mm diameter were cut from the bulk material by an ultrasonic cutter (Gatan). In order to reduce time of ion milling, in the last step of the mechanical thinning procedure, each 3 mm disk was mechanically thinned in a central area by a Dimple Grinder (Gatan). Final thinning was carried out by an ion beam system (Gatan PIPS) using Ar ions at 5 kV.

Samples (lamellae) for STEM, HR(S)TEM and EDX analyses were prepared by Focused Ion Beam (FIB) technique by the ZEISS NEON CrossBeam 40EsB microscope. Before milling, a layer of Pt was deposited at the place of cutting in order to protect the thin sample against heavy Ga ions during the preparation. Final milling was performed with the 4 keV Ga+ beam.

3. Results

3.1 Roughness measurements

Roughness measurements provided values in the same range for all the specimens. The average value of the average roughness R_a was 6.69 μm, with a standard deviation (SD) of 1.83 μm. As to maximum roughness R_{max}, an average value of 44.62 μm (SD = 18.78 μm) was obtained.

3.2 Hardness and mechanical tests

Results of tensile and hardness tests on tensile specimens (TENS) are shown in table 4, separately for the different groups of samples (TENS_0, TENS_45, TENS_90). The average value (AV) is reported with the corresponding standard deviation (SD). All samples prove to have a HRC value around 40 independently on the axis orientation during production. Elongation at break is around 12% for all samples while a slight decrease in UTS is found between TENS_0 and TENS_90.

Table 4 about here

Results for flexural properties are listed in Table 5, separately for the untreated samples (FLEX) and for those that underwent the firing cycle ($FLEX_{FC}$). Average value (AV) and standard deviation (SD) as obtained from the experimental investigations are listed in Table 5 for hardness (HRC) and transverse rupture strength (TRS). In this case, results in Table 5 evidences a reduction of both hardness and strength of the flexural samples after the firing cycle.

Table 5 about here

Results of statistical tests relating mechanical properties of TENS and FLEX groups of samples are reported in Table 6 in terms of p-value, estimated by statistical analysis software tool. Table 6 confirms the statistical significance of the mechanical properties variations evidenced above.

Table 6 about here

3.3 Morphological and chemical characterization (SEM, EDX)

Morphology and size distribution of particles in the EOS Ti64 powder are shown in Figure 3. The SEM image in Figure 3a shows morphology and size of spherical particles in the Ti64 starting powder, while the histogram in Figure 3b reports the distribution of particles diameter.

Quantitative analysis of SEM images were carried out by ImageJ software (version 1.50b) [Rasband, 1997-2016] while statistical information on particles size were obtained by Origin [OriginPro 8.5, OriginLab Corporation, One Roundhouse Plaza, Northampton, MA 01060 USA]. Particles diameter ranges from 0.7 μm to 118 μm with an average size of 16 μm, as estimated from the image in Figure 3a.

Figure 3 about here

Chemical characterization of samples was carried out by EDX analysis performed during the SEM observations. At least, five different large areas at same magnification (~300 x) for each sample were investigated. EDX analysis performed on powder, on samples in the reference condition (FLEX) and after the firing cycle ($FLEX_{FC}$) provided the results shown in Table 7. It is worth to note, that for all samples the Al content is within the nominal range while the V content is always lower than expected, even in the powder.

Table 7 about here

3.4 Crystallographic characterization (XRD)

The crystallographic structure of samples was investigated by XRD. Results for powder and samples in the reference condition (FLEX) and after the firing cycle ($FLEX_{FC}$) are shown in Figure 4. At least two samples for each condition from the different groups were measured.

Figure 4 about here

Rietveld analysis of the XRD patterns, performed by the MAUD (Materials Analysis Using Diffraction) program [Lutterotti, 2010], allowed estimating the lattice parameters of phases present in each sample. Results of peak analysis are reported in Table 8 with experimental error provided by the Maud software. Last row in Table 8 reports the nominal lattice parameters from the International Centre for Diffraction Data (ICDD) of α-Ti (card n. 44-1294) and β-Ti (card n. 44-1288), respectively.

Table 8 about here

Powder composition is 100% hexagonal (hcp) low temperature α phase. Same composition (100% hcp α) is found in the FLEX sample. Only after the firing cycle ($FLEX_{FC}$) a small peak at $2\theta=39.46°$ (full square in Figure 4) attributable to the cubic (bcc) high temperature β phase is present in addition to the α diffraction peaks. The lattice parameters calculated from the experimental XRD patterns are compared to nominal values in the ICDD cards, shown in the last row of Table 8.

Rietveld analysis performed on the XRD pattern of the $FLEX_{FC}$ sample provided a β phase volume content of about 10%.

3.5 Transmission electron microscopy (TEM, HRTEM, STEM) and microanalysis (EDX)

Figure 5 shows results of TEM observations performed on FLEX (figure 5a) and $FLEX_{FC}$ (figure 5b) samples.

Figure 5 about here

The FLEX sample (figure 5a) shows an acicular microstructure with a high density of dislocations inside the lamellar grains and rare twins.

In the $FLEX_{FC}$ sample (figure 5b) rare equiaxed grain with size up to 1 μm are present although the lamellar morphology is generally retained. Independently on the grain shape, the dislocation density in the $FLEX_{FC}$ sample is always heavily lower than in the FLEX sample (Figure 5). A further difference between samples in figure 5 is the presence of β phase at the plate boundaries of the $FLEX_{FC}$ sample (figure 5b). The β phase forms as elongated layers at the plate boundaries, with variable length up to 2 μm and width up to 100 nm (figure 5b). It is worth to note that the β layers at plate boundaries do not form a continuous net around the α plates (figure 5b). HRTEM observations performed at plate boundaries allowed studying the crystallographic relationships between α and β phases, confirming the Burgers relationships [Burgers, 1934].

Information about elements content and distribution inside α and β phases were obtained by STEM observations and EDX microanalysis. For the FLEX sample, where the β phase is absent, results showed a uniform distribution of Al and V inside the entire specimen and EDX analysis provided the elements concentration reported in Table 9. On the contrary, for the $FLEX_{FC}$ sample, STEM observations performed in high angle annular dark field (HAADF) mode and EDX elemental mapping showed segregation of V at the plate boundaries in correspondence of the β phase. Figure

6 reports results of STEM investigations and EDX mapping performed with signals from Ti, V and Al.

The STEM-HAADF image (figure 6a) evidences compositional contrast preferentially located at the plate boundaries. In particular, well-defined brighter zones not continuously connected are visible at the plate boundaries in figure 6a. The EDX elemental map obtained with signals from Ti, V and Al, performed on the same area of the sample, shows high V concentration in correspondence of the brighter zones (figure 6b). HRTEM observations and selected area electron diffraction (SAED) investigations showed that the V enriched zones are fully composed of β phase.

Figure 6 about here

Distribution of single elements in the same zone of the $FLEX_{FC}$ sample is reported in figures 6c-6e, for Ti, V and Al, respectively. In figures 6c-6e, brighter regions of the image are enriched with the corresponding element used for mapping.

EDX analysis performed in spot mode during the STEM observations allowed estimating the local concentration of elements in different zones of samples. Results obtained for FLEX and $FLEX_{FC}$ samples are shown in Table 9 where for the $FLEX_{FC}$ sample are reported results for both α and β phases. At least five measurements were performed on each phase present in the sample, and the element concentration in Table 9 is expressed as the average value with corresponding standard deviation.

Table 9 about here

It is worth to note the high concentration of V in the β phase suggesting element partitioning during the $\alpha \rightarrow \beta$ transformation induced by firing cycle.

4. Discussion

The Ti alloy considered in this study is the well-known Ti-6Al-4V alloy commonly used in industrial applications, and specifically developed by EOS GmbH Electro Optical System for biomedical applications. Nominal composition of the alloy, provided by the manufacturer, is within the standard compositional range with low content of Fe, H and C (Table 2).

The laser sintering process carried out by using the parameters reported in Table 1 allowed producing tensile (TENS) and flexural (FLEX) samples for the mechanical tests and the structural characterization. After production and thermal treatment at 800 °C for 4 hours (HT), all samples are compact without any visible porosity, with an average surface roughness R_a=6.69 μm. Average surface roughness around the same value was measured also for the $FLEX_{FC}$ group of samples.

Mechanical tests performed on the TENS samples produced in different building orientation show average values of UTS in the range 1080-1110 MPa, with elongations of about 12% (Table 4). All groups proved to have good test repeatability with a very low standard deviation. Regarding tensile strength, although the span among results for different orientations is only 30 MPa, yet the t-test proves the statistical significance of the difference between the groups TENS_0 and TENS_90 (Table 6). On the contrary, no significant effect of build orientation is observed on ductility (Table 4). If compared the nominal values stated by the producer, strength is well above expectations, while elongation at break is slightly lower (Table 3).

Effects of build orientation on the mechanical properties of Ti-6Al-4V alloy are reported for both laser sintering [Wauthele et al., 2015] and electron beam melting [Antonysamy et al., 2013] technologies. Inhomogeneity occurs for the high thermal gradients developed during the production process that could induce crystallographic textures capable of influencing the mechanical behavior of the material along specific orientations [Thjis et al., 2013].

Post-production processes consisting of mechanical and/or thermal treatments are commonly used to reduce effects of build orientation [Wauthele et al., 2015; Antonysamy et al., 2013]. However, in most cases, such post-production treatments induce variation in microstructure and consequently in

mechanical properties [Thjis et al., 2010, 2013; Vrancken et al., 2012]. In our case, results in Table 4 show that the HT treatment carried out soon after production is not sufficient to remove the structural inhomogeneity causing UTS reduction in the TENS_90 sample. However, the residual inhomogeneity in the TENS_90 sample does not produce any effect on the elongation behavior of the alloy (Table 4 and Table 6).

The experimental values of UTS and elongation obtained in this study (Table 4) are within the range reported in literature for both conventional and additive production technologies [Murr et al., 2009a, 2009b; Matsumoto et al., 2011a; Leunders et al., 2013] and are even comparable to the values obtained by Xu et al. (2015) after in situ martensite decomposition that produces an ultrafine lamellar α+β structure.

Flexural samples exhibit excellent mechanical properties too, even after the firing cycle that reduces both hardness and strength. In fact, as shown in Table 5 flexural strength in the untreated condition is as high as 2566 MPa, and decreases to 2359 MPa because of the firing operation. At the same time, hardness goes from 45 to 40 HRC. Both variations are statistically significant, as shown in Table 6.

In terms of microstructure, whose modification produce variation in the mechanical response, the FLEX sample shows the typical α' acicular microstructure of metal parts subject to high cooling rates [Murr et al., 2009a; Matsumoto et al., 2011a], with a high density of dislocations inside the lamellar grains and rare twins (Figure 5a). The FLEX sample is completely formed of α' phase with an hcp crystallographic structure and lattice parameters identical to the Ti64 powder (Table 8), even though the average content of V is slightly lower (2.5 wt%) with respect to the powder (3.3 wt%), as shown in Table 7. This latter result is further confirmed by STEM-EDX analysis performed in spot mode reported in Table 9, which shows values of element content in complete agreement with those obtained by SEM-EDX on large areas of the sample (Table 7). Probably, a small amount (<1 wt%) of V is lost during the laser melting process, but this is not enough to cause modifications of the crystallographic lattice parameters (Table 8). Furthermore, from the experimental results in

Table 8 it is evident that the crystallographic cell of the hcp α' phase, in powder and FLEX sample, is smaller than the crystallographic cell of the nominal hcp α-Ti phase reported in the ICDD card (Table 8).

After the firing cycle, microstructure and mechanical behavior of the alloy strongly change. Hardness and strength decrease of about 9% and 8%, respectively (Table 5). In terms of microstructure, although the average composition (Table 7) of the sample ($FLEX_{FC}$) is unaltered with respect to the untreated condition (FLEX), XRD investigations show the presence of the bcc β phase in addition to the hcp α phase (Figure 4). TEM observations show β phase located at the plate boundaries of α grain (Figure 5b) and confirm the Burgers orientation relationships between the two phases. The volume fraction of the β phase (about 10%) estimated by Rietveld analysis of XRD pattern was confirmed by STEM-HAADF observations. Attallah et al. (2009) have already demonstrated that combination of XRD and electron microscopy techniques for the estimation of the α/β phase fraction in α+β Ti alloys is a very reliable method.

Calculation of lattice parameters from the XRD pattern (Figure 4) shows an increase of the hcp α lattice parameters (Table 8) in the treated sample ($FLEX_{FC}$) with respect to the untreated one (FLEX). In particular, the lattice parameter a increases of about 0.3% while c of about 0.5% (Table 8). On the contrary, measured value of the bcc β phase lattice parameter is a=0.323±0.002 nm, about 2% lower than the nominal value reported in the ICDD card (Table 8).

Modification of mechanical behavior in Ti-Al-V alloys as a consequence of shape and crystallography of the constituent phases has been already observed [Matsumoto et al., 2011b, 2011c]. In particular, Matsumoto et al. (2011c) ascribed the excellent ductility of their Ti-6Al-4V alloy to: a) the single phase hcp (α, α') constituent, b) the fine equiaxed morphology, c) the enrichment of V content and the decrease in Al content of α' martensitic regions during solution treatment.

In our case, the lamellar structure of the α phase is substantially retained after the firing cycle while the volume fraction of the β phase (about 10%) is limited, therefore the strength reduction observed in our alloy can be only partially attributed to the phase type and morphology in the treated sample.

On the other hand, STEM-HAADF observations and STEM-EDX analysis evidenced a strong partitioning of elements between the β phase at the plate boundaries and the α plates (Figure 6). Results in Table 9 for the $FLEX_{FC}$ sample clearly show an enrichment of V in the β phase and a slight increase of Al in the α phase. It is worth to note the high concentration of V (about 20 wt%) and the reduced content of Al (about 3 wt%) in the β phase, as well as the low V content (<2 wt%) in the α phase (Table 9). These results suggest a diffusion controlled mechanism responsible of β formation at the grain boundaries (Figure 6).

Diffusion processes responsible of the α ↔ β transformations in Ti-6Al-4V alloy are already reported in literature [Barriobero-Vila et al., 2015; Semiatin et al., 2004]. In α+β systems, it was shown that since the diffusivity of V in β is lower than in α, diffusion of V in α produces first an enrichment of the α grain boundaries to which follows a gradual diffusion of V atoms into β [Semiatin et al., 2004]. On the other hand, Barriobero-Vila et al. (2015), in α+β systems, supposed the contemporary diffusion of V into β and Ti into α to justify the observed variations of lattice parameters of the two phases. Thermodynamic calculation demonstrated that also diffusion of Al from α into β can occur during the α → β transformation [Elmer et al., 2004]. Furthermore, close relationship between variation of lattice parameters and diffusion mechanisms in α and β phases as well as lattice strain relaxation have been reported [Elmer et al., 2005a, 2005b; Swarnakar et al., 2011; Banerjee et al., 2003; Lieblich et al., 2016].

Lastly, it must be stressed that the content of V in the β phase (~20 wt%) found in our alloy largely exceeds the value of 15 wt% needed to retain the β phase at room temperature in binary Ti-V systems [Lutjering and Williams, 2007].

Therefore, the experimental results obtained in the current work indicate that, during the firing cycle, atoms of V diffuse inside the α phase and accumulate at the plate boundaries where the α →

β transformation starts. Diffusion mechanisms involving Al and Ti between the newly formed β and α cannot be excluded at this stage. Hence, the combined effects of β phase formation at the plate boundaries and the variation of lattice parameters of α, due to the diffusional processes, are responsible of the modified mechanical behavior of the material after the firing cycle.

5. Conclusions

A Ti-6Al-4V alloy for biomedical applications produced by laser sintering of the EOS Ti64 powder was submitted to mechanical tests and microstructural characterization. Effects of building orientation and thermal treatments on mechanical and structural properties of the alloy were investigated. Thermal treatments consist of a firing cycle that simulate veneering of metal parts with ceramics. The main results obtained in this study can be summarized as follows:

- Samples are compact without any visible porosity, with an average surface roughness independent on building orientation and thermal treatment;
- Samples not submitted to the firing cycle are single phase acicular α';
- Effects of building direction on the mechanical behavior were evidenced for tensile samples produced with axis in Y direction with respect to samples with axis in horizontal direction (X), which is the slide direction of the recoater;
- Samples submitted to the firing cycle show reduced values of strength with respect to the untreated samples due to the combined effects of formation of β phase at the α plate boundaries and variation of lattice parameters of α;
- The β phase forms at the boundaries of α plates as single laths not continuously connected;
- Element partitioning during thermal treatments is the main effect responsible of enrichment with V atoms (up to 20 wt%) of the α plate boundaries where the formation of β takes place.

Diffusion of atoms (Al, Ti) between α and β phases is probably responsible of the lattice parameter variations measured in this study.

Although, the firing cycle induces modifications in the mechanical behavior of metal parts produced by laser sintering, values of hardness, strength and ductility of the Ti-6Al-4V alloy considered in this study remain well above the accepted values for applications.

Acknowledgements

The research leading to these results has received funding from the European Union Seventh Framework Programme under Grant Agreement 312483 - ESTEEM2 (Integrated Infrastructure Initiative–I3). The authors kindly acknowledge MSc. Adam Gruszczynski (AGH-UST) and A. Di Cristoforo (UNIVPM) for FIB lamellae and TEM sample preparation.

References

Ahmed, T., Rack, H.J., 1998. Phase transformations during cooling in α+β titanium alloys, Mat. Sci. Eng. A243, 206-211.

Ahmed, A.A., Mhaede, M., Wollmann, M., Wagner, L., 2016. Effect of micro shot peening on the mechanical properties and corrosion behavior of two microstructure Ti–6Al–4V alloy. Appl. Surf. Sci. 363, 50–58.

Antonysamy, A.A., Meyer, J., Prangnell, P.B. 2013. Effect of build geometry on the β-grain structure and texture in additive manufacture of Ti-6Al-4V by selective electron beam melting, Mater. Character. 84, 153-168.

Attallah, M.M., Zabeen, S., Cernik, R.J., Preuss, M., 2009. Comparative determination of the α/β phase fraction in α+β-titanium alloys using X-ray diffraction and electron microscopy. Mater. Charact. 60, 1248-1256.

Banerjee, R., Collins, P.C., Bhattacharyya, D., Banerjee, S., Fraser, H.L.. 2003. Microstructural evolution in laser deposited compositionally graded α/β titanium-vanadium alloys. Acta Mater. 51, 3277–3292.

Barriobero-Vila, P., Requena, G., Buslaps, T., Alfeld, M., Boesenberg, U., 2015. Role of element partitioning on the α–β phase transformation kinetics of a bi-modal Ti–6Al–6V–2Sn alloy during continuous heating. J. Alloys Comp. 626, 330–339.

Burgers, W.G., 1934. On the process of transition of the cubic-body-centered modification into the hexagonal-close-packed modification of zirconium. Physica 1, 561-586.

Elmer, J.W., Palmer, T.A., Babu, S.S., W. Zhang, W., T. DebRoy, T., 2004. Phase transformation dynamics during welding of Ti–6Al–4V. J. Appl. Phys. 95, 8327.

Elmer, J.W., Palmer, T.A., Babu, S.S., Specht, E.D., 2005a. In situ observations of lattice expansion and transformation rates of α and β phases in Ti–6Al–4V. Mat. Sci. Eng. A 391, 104–113.

Elmer, J.W., Palmer, T.A., Babu, S.S., Specht, E.D., 2005b. Low temperature relaxation of residual stress in Ti–6Al–4V. Scripta Mater. 52, 1051–1056.

Leuders, S., Thöne, M., Riemer, A., Niendorf, T., Tröster, T., Richard, H.A., Maier, H.J., 2013. On the mechanical behaviour of titanium alloy TiAl6V4 manufactured by selective laser melting: Fatigue resistance and crack growth performance. Int. J. Fatigue 48, 300–307.

Lieblich, M., Barriuso, S., Multigner, M., Gonzalez-Doncel, G., Gonzalez-Carrasco, J.L., 2016. Thermal oxidation of medical Ti6Al4V blasted with ceramic particles: Effects on the

microstructure, residual stresses and mechanical properties. J. Mech. Behav. Biomed. Mater. 54, 173-184.

Lutjering, G., Williams, J.C., 2007. Titanium, second ed. Springer-Verlag, Berlin.

Lutterotti, L., 2010. Total pattern fitting for the combined size-strain-stress-texture determination in thin film diffraction. Nucl. Inst. Meth. Phys. Res. B 268, 334-340.

Matsumoto, H., Yoneda, H., Sato, K., Kurosu, S., Maire, E., Fabregue, D., Konno, T.J., Chiba, A., 2011a. Room-temperature ductility of Ti–6Al–4V alloy with α' martensite microstructure. Mat. Sci. Eng. A 528, 1512–1520.

Matsumoto, H., Yoneda, H., Fabregue, D., Maire, E., Chiba, A., Gejima, F., 2011b. Mechanical behaviors of Ti–V–(Al, Sn) alloys with α' martensite microstructure. J. Alloys Comp. 509, 2684-2692.

Matsumoto, H., Yoneda, H., Sato, K., Kurosu, S., Maire, E., Fabregue, D., Konno, T.J., Chiba, A., 2011c. Room-temperature ductility of Ti–6Al–4V alloy with α' martensite microstructure. Mat. Sci. Eng. A 528, 1512–1520.

Matsumoto, H., Nishihara, T., Iwagaki, Y., Shiraishi, T., Ono, Y., Chiba, A., 2016. Microstructural evolution and deformation mode under high-temperature-tensile-deformation of the Ti-6Al-4V alloy with the metastable α′ martensite starting microstructure, Mat. Sci. Eng. A661, 68–78

Murr, L.E., Quinones, S.A., Gaytan, S.M., Lopez, M.I., Rodela, A., Martinez, E.Y., Hernandez, D.H., Martinez, E., Medina, F., Wicker, R.B., 2009a. Microstructure and mechanical behavior of

Ti–6Al–4V produced by rapid-layer manufacturing, for biomedical applications. J. Mech. Behav. Biomed. Mater. 2, 20-32.

Murr, L.E., Esquivel, E.V., Quinones, S.A., Gaytan, S.M., Lopez, M.I., Martinez, E.Y., Medina, F., Hernandez, D.H., Martinez E., Martinez, J.L., Stafford, S.W., Brown, D.K., Hoppe, T., Meyers, W., Lindhe, U., Wicker, R.B., 2009b. Microstructures and mechanical properties of electron beam-rapid manufactured Ti–6Al–4V biomedical prototypes compared to wrought Ti–6Al–4V. Mater. Charact. 60, 96-105.

Polmear, I.J., 2006. Light Alloys, fourth ed. Elsevier Ltd, Oxford.

Rasband, W.S., ImageJ, U.S. National Institutes of Health, Bethesda, Maryland, USA, http://imagej.nih.gov/ij/, 1997-2016.

Semiatin, S.L., Brown, T.M., Goff, T.A., Fagin, P.N., Barker, D.R., Turner, R.E., Murry, J.M., Miller, J.D., Zhang, F., 2004. Diffusion coefficients for modeling the heat treatment of Ti–6Al–4V. Metall. Mater. Trans. A 35, 3015–3018.

Shamsaeia, N., Yadollahi, A., Bian, L., Thompson, S.M., 2015. An overview of Direct Laser Deposition for additive manufacturing; Part II: Mechanical behavior, process parameter optimization and control. Additive Manufacturing 8, 12–35.

Song, B., Dong, S., Zhang, B., Liao, H., Coddet, C., 2012. Effects of processing parameters on microstructure and mechanical property of selective laser melted Ti6Al4V. Materials and Design 35, 120–125.

Swarnakar, A.K., Van der Biest, O., Baufeld, B., 2011. Thermal expansion and lattice parameters of shaped metal deposited Ti–6Al–4V. J. Alloys Comp. 509, 2723–2728.

Thijs, L., Verhaeghe, F., Craeghs, T., Van Humbeeck, J., Kruth, J.P., 2010. A study of the microstructural evolution during selective laser melting of Ti–6Al–4V. Acta Mater. 58, 3303–3312.

Thijs, L., Montero Sistiaga, M.L., Wauthle, R., Xie, Q., Kruth, J.P., Van Humbeeck, J., 2013. Strong morphological and crystallographic texture and resulting yield strength anisotropy in selective laser melted tantalum. Acta Mater. 61, 4657–68.

Valiev, R.Z., Alexandrov, I.V., Zhu, Y.T., Lowe, T.C., 2002. Paradox of strength and ductility in metals processed by severe plastic deformation, Journal of Materials Research 17, 5-8.

Vrancken, B., Thijs, L., Kruth, J.P., Van Humbeeck, J., 2012. Heat treatment of Ti6Al4V produced by Selective Laser Melting: Microstructure and mechanical properties. J. Alloys Comp. 541, 177–185.

Wauthle, R., Vrancken, B., Beynaerts, B., Jorissen, K., Schrooten, J., Kruth, J.P., Van Humbeeck, J., 2015. Effects of build orientation and heat treatment on the microstructure and mechanical properties of selective laser melted Ti6Al4V lattice structures. Additive Manufacturing 5, 77–84.

Wu, S.Q., Lu, Y.J., Gan, Y.L., Huang, T.T., Zhao, C.Q., Lin, J.J., Guo, S., Lin, J.X., 2016. Microstructural evolution and microhardness of a selective-laser melted Ti-6Al-4V alloy after post heat treatments. J. Alloys Comp. 672, 643-652.

Xu, W., Brandt, M., Sun, S., Elambasseril, J., Liu, Q., Latham, K., Xia, K., Qian, M., 2015. Additive manufacturing of strong and ductile Ti–6Al–4V by selective laser melting via in situ martensite decomposition. Acta Mater. 85, 74–84.

Zeng, L., Bieler, T.R., 2005. Effects of working, heat treatment, and aging on microstructural evolution and crystallographic texture of α, α', α" and β phases in Ti–6Al–4V wire, Mat. Sci. Eng. A392, 403–414.

Zherebtsov, S., Salishchev, G., Galeyev, R., Maekawa, K., 2005. Mechanical properties of Ti–6Al–4V titanium alloy with submicrocrystalline structure produced by severe plastic deformation. Mater. Trans. 46, 2020-2025.

Figure and table captions

Figure 1 Geometry of samples produced for mechanical tests: a) flexural (FLEX), b) tensile (TENS_0). Dimensions in mm.

Figure 2 Thermal cycle used for fire simulation. The cooling phase between each firing step is not represented.

Figure 3 EOS Ti64 powder: a) SEM image, b) size distribution of particle diameter.

Figure 4 XRD patterns of powder, sample in the reference condition (FLEX) and after the firing cycle ($FLEX_{FC}$).

Figure 5 TEM-BF images: a) flexural sample in the reference condition (FLEX) and b) after the firing cycle ($FLEX_{FC}$).

Figure 6 STEM-HAADF image of the $FLEX_{FC}$ sample and corresponding elemental mapping performed with signals from Ti, V and Al: a) HAADF image, b) EDX map obtained by combining signals from Ti, V and Al, c) EDX map of Ti, d) EDX map of V and e) EDX map of Al. (Color references in the web version of the paper).

Table 1 Sintering parameters used for DMLS.

Table 2 Nominal composition of EOS Ti64 powder.

Table 3 Material properties as reported in the material datasheet for the as sintered (AS) material and after thermal treating at 800 °C for 4 hours in argon atmosphere (HT).

Table 4 Average value (AV) and standard deviation (SD) of ultimate tensile strength (UTS), strain at break (ε_b) and Rockwell C hardness (HRC) of the tensile specimens (TENS).

Table 5 Average value (AV) and standard deviation (SD) of Rockwell C hardness (HRC) and transverse rupture strength (TRS) of the flexural specimens.

Table 6 p-values resulting from the t-test for the variables UTS, ε_b, HRC and TRS among the different groups of samples. Records below the level of significance of 0.05 are underlined.

Table 7 Element concentration (in wt%) obtained from SEM-EDX analysis of powder and samples in the reference condition (FLEX) and after the firing cycle ($FLEX_{FC}$).

Table 8 Experimental lattice parameters calculated from peak position in the XRD patterns. Last row reports the nominal lattice parameter values from cards of the International Centre for Diffraction Data (ICDD).

Table 9 Average value and standard deviation from five measurements of element concentration in α-Ti and β-Ti phases obtained by STEM-EDX analysis performed in spot mode on both FLEX and $FLEX_{FC}$ samples. All values are in wt%.

Table 1

Table 1 Sintering parameters used for DMLS.

Laser power	200 W
Laser spot diameter	200 µm
Scan speed	up to 7.0 m/s
Building speed	2 - 20 mm^3/s
Layer thickness	20 µm
Protective atmosphere	Oxygen (max 1.5%)

Table 2

Table 2 Nominal composition of EOS Ti64 powder.

Al (wt.%)	V (wt.%)	O (ppm)	N (ppm)	C (ppm)	H (ppm)	Fe (ppm)	Ti
5.50 - 6.75	3.50 - 4.50	< 2000	< 500	< 800	< 150	< 3000	Balance

Table 3

Table 3 Material properties as reported in the material datasheet for the as sintered (AS) material and after thermal treating at 800 °C for 4 hours in argon atmosphere (HT).

	AS	**HT**
Density [g/cm^3]	4.41	
UTS [MPa]	1230 ± 50	1050 ± 20
$R_{p0.2}$ [MPa]	1060 ±50	1000 ± 20
Elongation at break [%]	10 ± 2	14 ± 1
Young's Modulus [GPa]	110 ± 10	116 ± 10
Hardness (HRC)	41-44	

Table 4

Table 4 Average value (AV) and standard deviation (SD) of ultimate tensile strength (UTS), strain at break (ε_b) and Rockwell C hardness (HRC) of the tensile specimens (TENS).

	UTS (MPa)		ε_b (%)		HRC	
	AV	SD	AV	SD	AV	SD
TENS_0	1110	1	12	2	39.8	2.6
TENS_45	1098	26	13	1	38.7	3.9
TENS_90	1080	6	11	1	38.9	2.5

Table 5

Table 5 Average value (AV) and standard deviation (SD) of Rockwell C hardness (HRC) and transverse rupture strength (TRS) of the flexural specimens.

	HRC		TRS (MPa)	
	AV	SD	AV	SD
FLEX	44.9	0.6	2566	39.3
$FLEX_{FC}$	40.7	2.7	2359	28.7

Table 6

Table 6 p-values resulting from the t-test for the variables UTS, ε_b, HRC and TRS among the different groups of samples. Records below the level of significance of 0.05 are underlined.

	p-values			
	UTS (MPa)	ε_b (%)	HRC	TRS
TENS_0 - TENS_45	0.36	0.36	0.29	-
TENS_0 - TENS_90	0.00	0.70	0.26	-
TENS_45 - TENS_90	0.30	0.14	0.86	-
$FLEX_{FC}$ -FLEX	-	-	0.00	0.00

Table 7

Table 7 Element concentration (in wt%) obtained from SEM-EDX analysis of powder and samples in the reference condition (FLEX) and after the firing cycle ($FLEX_{FC}$).

Sample	Al	V	Ti
Powder	6±1	3.3±0.3	91±7
FLEX	6±1	2.5±0.3	92±7
$FLEX_{FC}$	6±1	2.5±0.3	91±7

Table 8

Table 8 Experimental lattice parameters calculated from peak position in the XRD patterns. Last row reports the nominal lattice parameter values from cards of the International Centre for Diffraction Data (ICDD).

Sample	**α-Ti (nm)**	**β-Ti (nm)**
Powder	a = 0.2922 ± 0.0001 c = 0.4659 ± 0.0001	-
FLEX	a = 0.2922 ± 0.0002 c = 0.4658 ± 0.0004	-
$FLEX_{FC}$	a = 0.2930 ± 0.0001 c = 0.4681 ± 0.0003	a = 0.323 ± 0.002
Nominal	a = 0.29505 c = 0.46826 ICDD card n. 44-1294	a = 0.33065 ICDD card n. 44-1288

Table 9

Table 9 Average value and standard deviation from five measurements of element concentration in α-Ti and β-Ti phases obtained by STEM-EDX analysis performed in spot mode on both FLEX and $FLEX_{FC}$ samples. All values are in wt%.

Sample	Ti phase	Al	V	Ti
FLEX	α	6.10±0.03	2.786±0.001	91.12±0.16
$FLEX_{FC}$	α	6.49±0.04	1.95±0.24	91.6±0.3
$FLEX_{FC}$	β	2.77±0.18	20.3±0.5	76.95±0.24

Figure 1

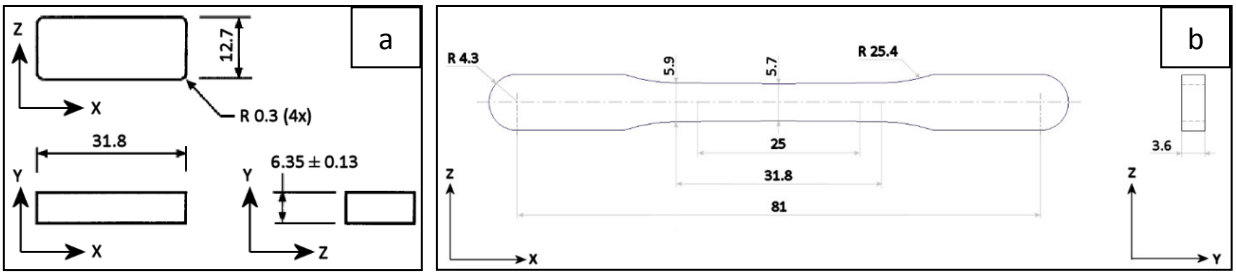

Figure 1 Geometry of samples produced for mechanical tests: a) flexural (FLEX), b) tensile (TENS_0). Dimensions in mm.

Figure 2

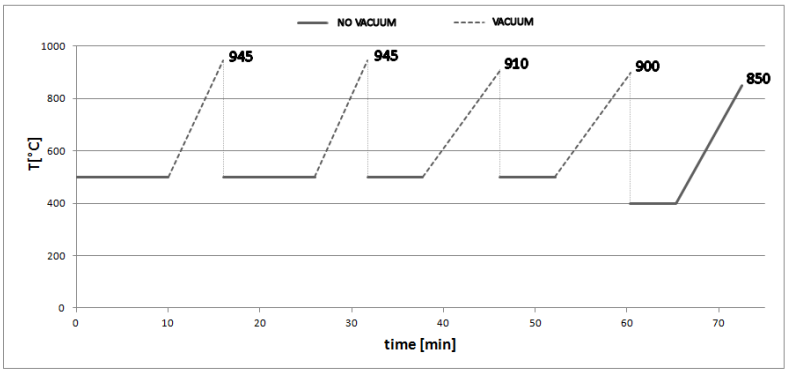

Figure 2 Thermal cycle used for fire simulation. The cooling phase between each firing step is not represented.

Figure 3

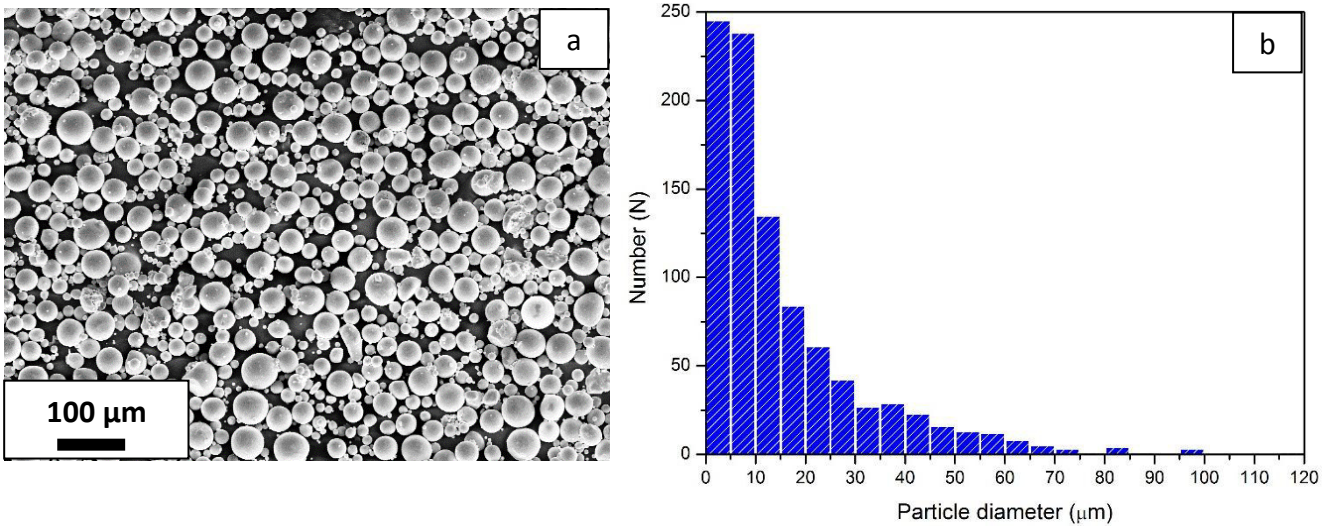

Figure 3 EOS Ti64 powder: a) SEM image, b) size distribution of particle diameter.

Figure 4

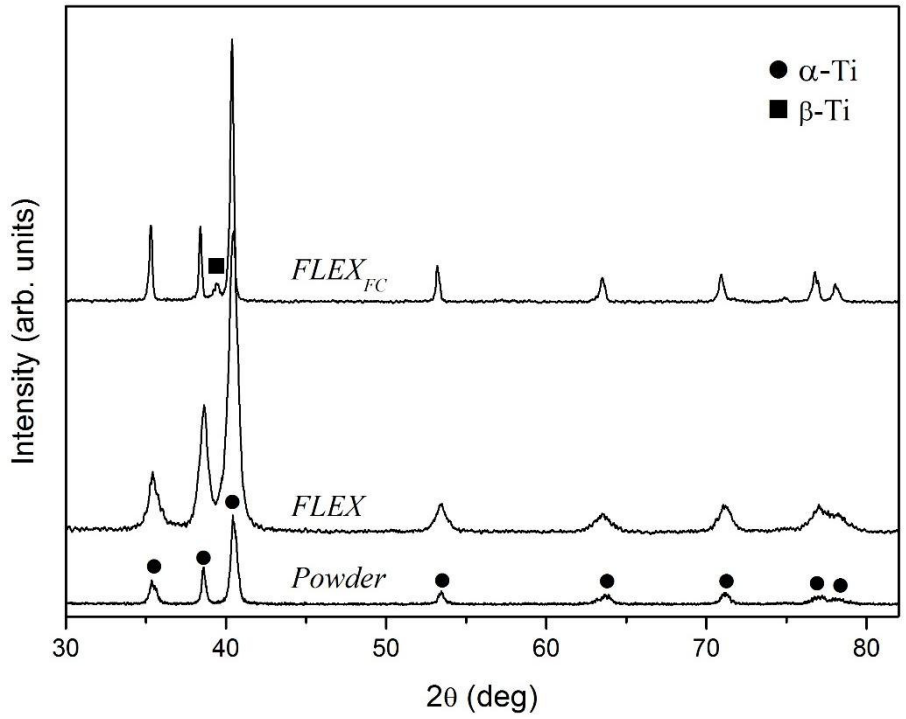

Figure 4 XRD patterns of powder, sample in the reference condition (FLEX) and after the firing cycle ($FLEX_{FC}$).

Figure 5

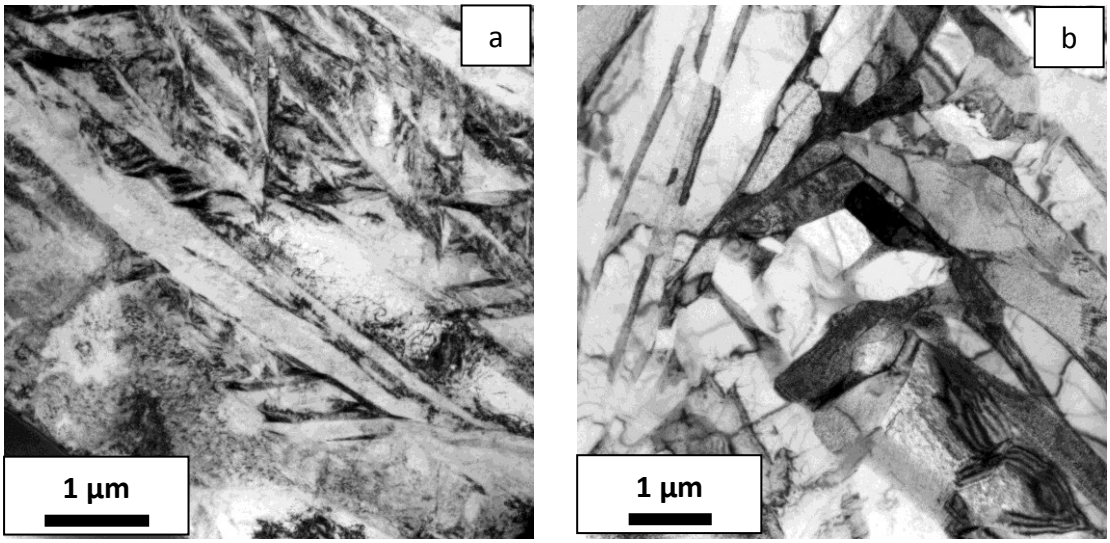

Figure 5 TEM-BF images: a) flexural sample in the reference condition (FLEX) and b) after the firing cycle ($FLEX_{FC}$).

Figure 6

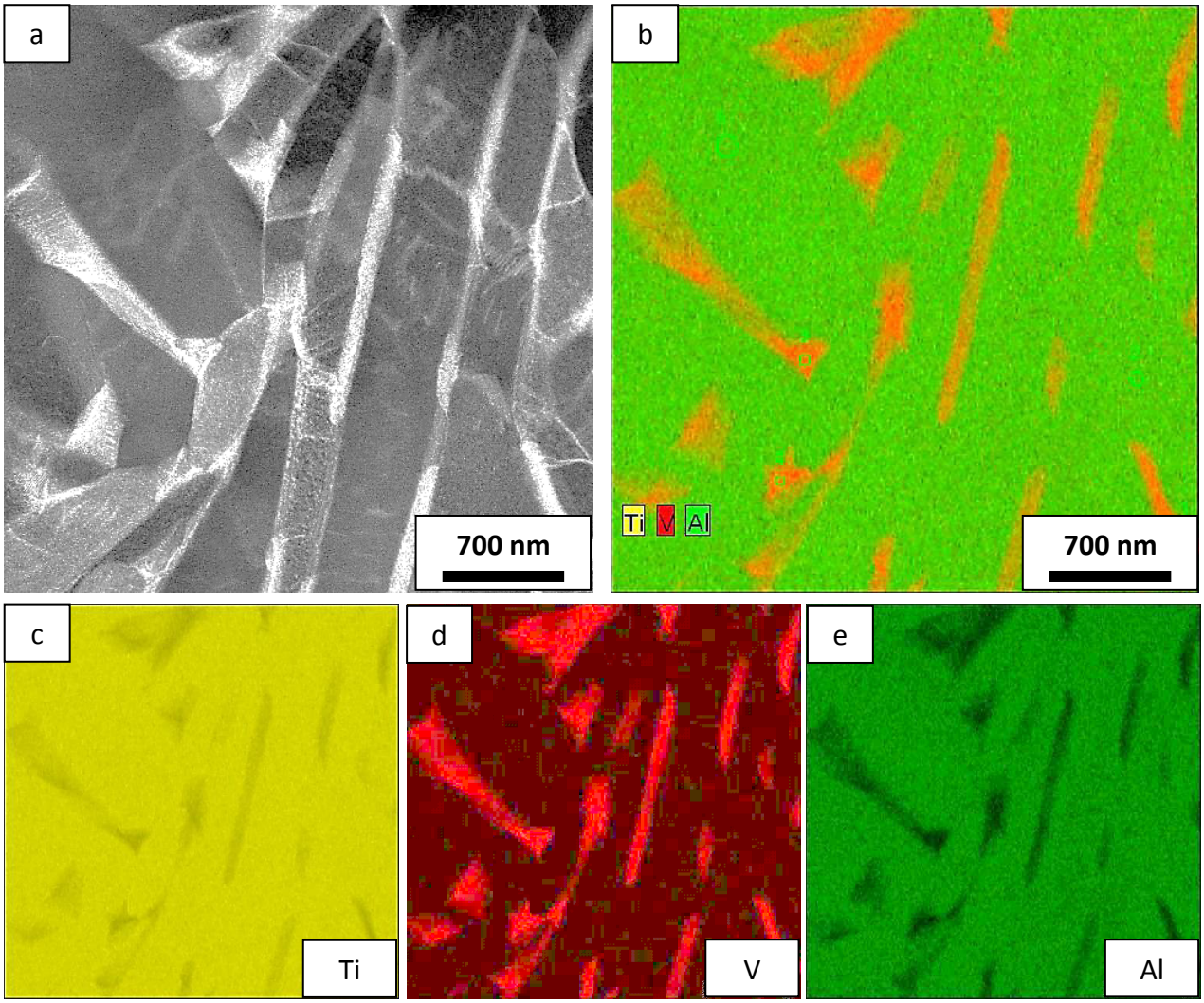

Figure 6 STEM-HAADF image of the $FLEX_{FC}$ sample and corresponding elemental mapping performed with signals from Ti, V and Al: a) HAADF image, b) EDX map obtained by combining signals from Ti, V and Al, c) EDX map of Ti, d) EDX map of V and e) EDX map of Al. (Color references in the web version of the paper).

Figure 1

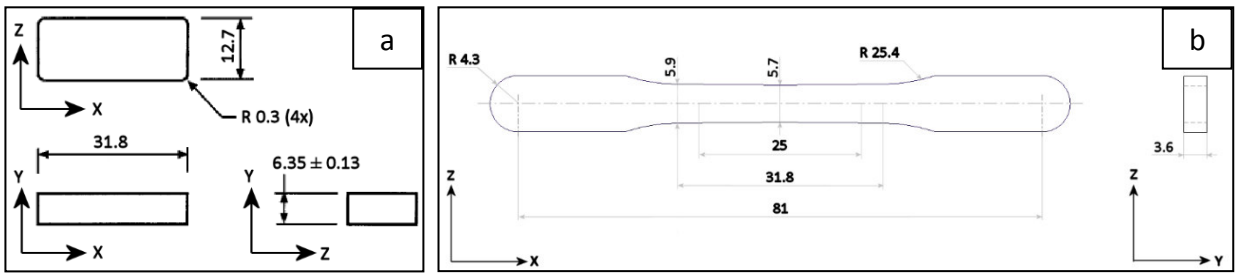

Figure 1 Geometry of samples produced for mechanical tests: a) flexural (FLEX), b) tensile (TENS_0). Dimensions in mm.

Figure 2

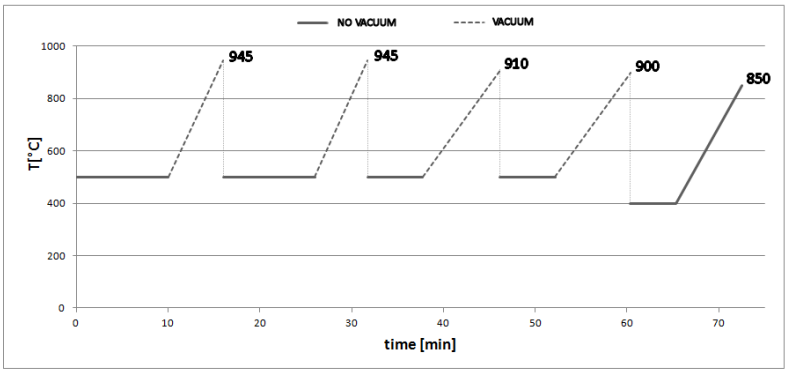

Figure 2 Thermal cycle used for fire simulation. The cooling phase between each firing step is not represented.

Figure 3

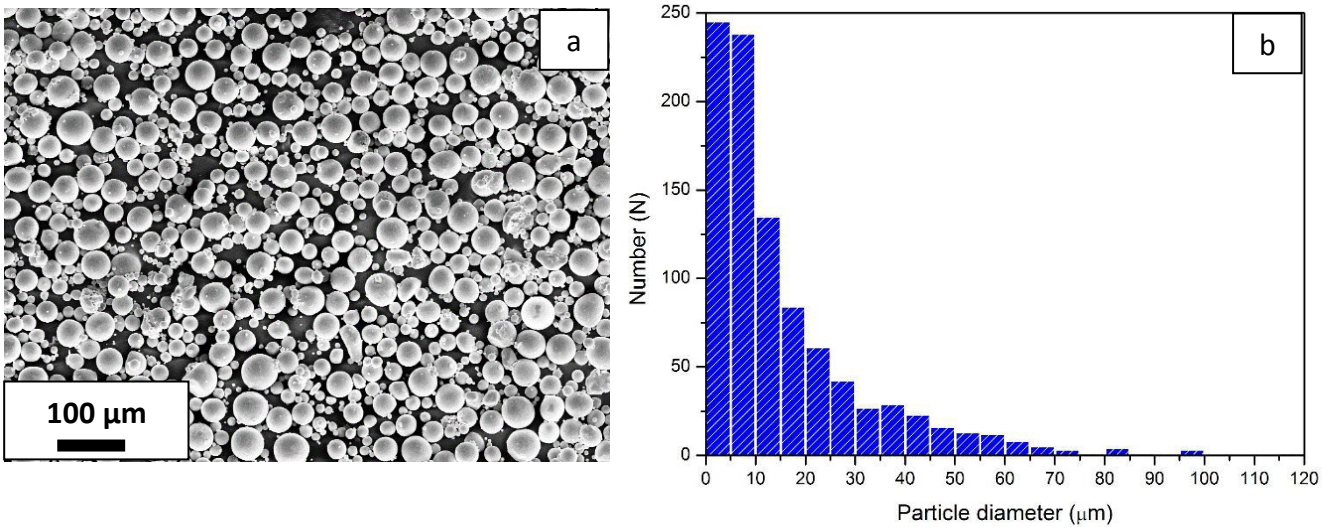

Figure 3 EOS Ti64 powder: a) SEM image, b) size distribution of particle diameter.

Figure 4

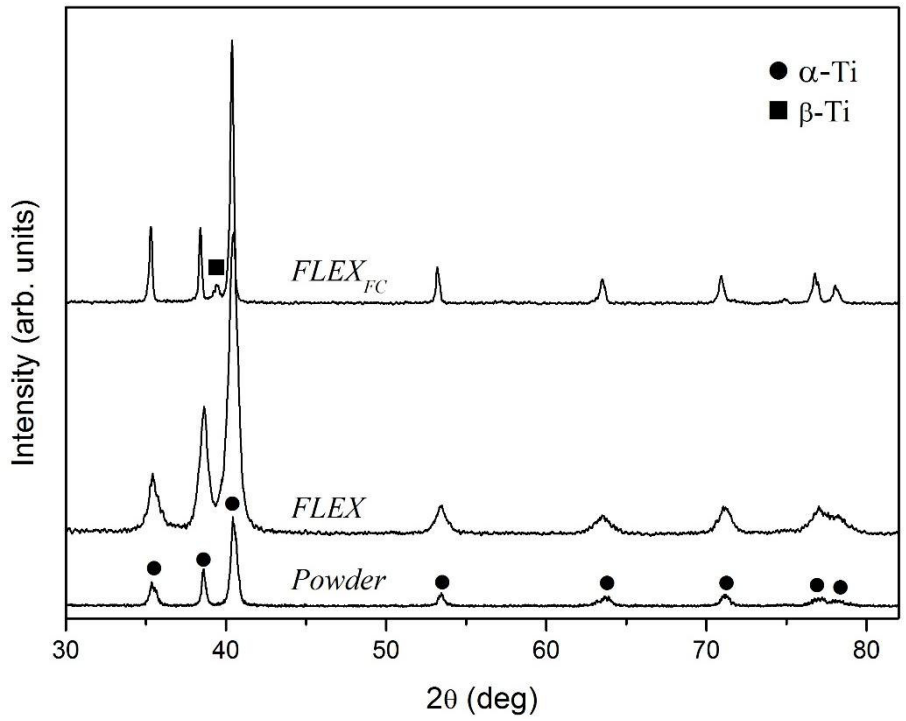

Figure 4 XRD patterns of powder, sample in the reference condition (FLEX) and after the firing cycle ($FLEX_{FC}$).

Figure 5

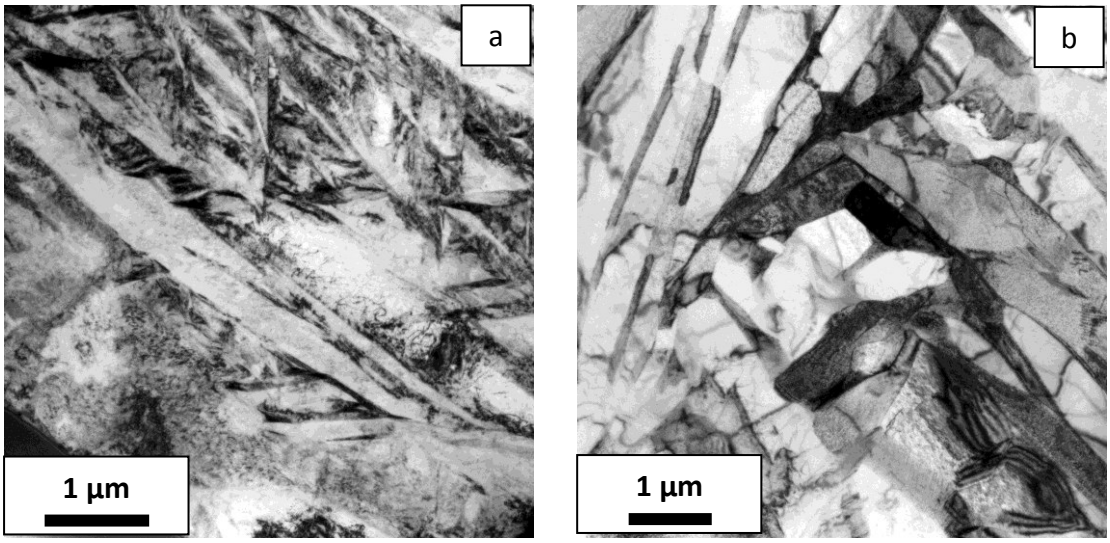

Figure 5 TEM-BF images: a) flexural sample in the reference condition (FLEX) and b) after the firing cycle ($FLEX_{FC}$).

Figure 6

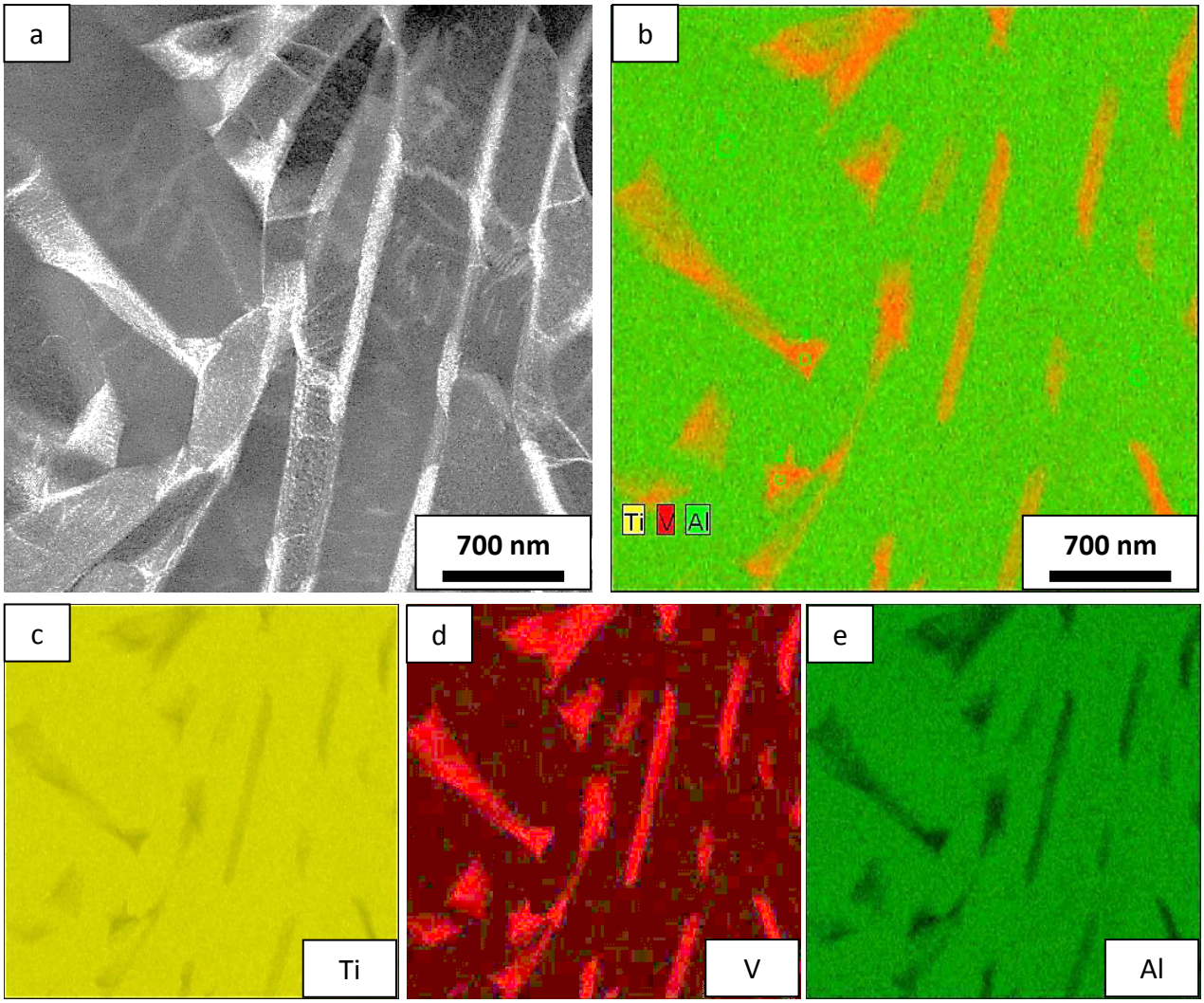

Figure 6 STEM-HAADF image of the $FLEX_{FC}$ sample and corresponding elemental mapping performed with signals from Ti, V and Al: a) HAADF image, b) EDX map obtained by combining signals from Ti, V and Al, c) EDX map of Ti, d) EDX map of V and e) EDX map of Al. (Color references in the web version of the paper).

Table 1

Table 1 Sintering parameters used for DMLS.

Laser power	200 W
Laser spot diameter	200 µm
Scan speed	up to 7.0 m/s
Building speed	2 - 20 mm^3/s
Layer thickness	20 µm
Protective atmosphere	Oxygen (max 1.5%)

Table 2

Table 2 Nominal composition of EOS Ti64 powder.

Al (wt.%)	V (wt.%)	O (ppm)	N (ppm)	C (ppm)	H (ppm)	Fe (ppm)	Ti
5.50 - 6.75	3.50 - 4.50	< 2000	< 500	< 800	< 150	< 3000	Balance

Table 3

Table 3 Material properties as reported in the material datasheet for the as sintered (AS) material and after thermal treating at 800 °C for 4 hours in argon atmosphere (HT).

	AS	**HT**
Density [g/cm^3]	4.41	
UTS [MPa]	1230 ± 50	1050 ± 20
$R_{p0.2}$ [MPa]	1060 ±50	1000 ± 20
Elongation at break [%]	10 ± 2	14 ± 1
Young's Modulus [GPa]	110 ± 10	116 ± 10
Hardness (HRC)	41-44	

Table 4

Table 4 Average value (AV) and standard deviation (SD) of ultimate tensile strength (UTS), strain at break (ε_b) and Rockwell C hardness (HRC) of the tensile specimens (TENS).

	UTS (MPa)		ε_b (%)		HRC	
	AV	SD	AV	SD	AV	SD
TENS_0	1110	1	12	2	39.8	2.6
TENS_45	1098	26	13	1	38.7	3.9
TENS_90	1080	6	11	1	38.9	2.5

Table 5

Table 5 Average value (AV) and standard deviation (SD) of Rockwell C hardness (HRC) and transverse rupture strength (TRS) of the flexural specimens.

	HRC		TRS (MPa)	
	AV	SD	AV	SD
FLEX	44.9	0.6	2566	39.3
$FLEX_{FC}$	40.7	2.7	2359	28.7

Table 6

Table 6 p-values resulting from the t-test for the variables UTS, ε_b, HRC and TRS among the different groups of samples. Records below the level of significance of 0.05 are underlined.

	p-values			
	UTS (MPa)	ε_b (%)	HRC	TRS
TENS_0 - TENS_45	0.36	0.36	0.29	-
TENS_0 - TENS_90	0.00	0.70	0.26	-
TENS_45 - TENS_90	0.30	0.14	0.86	-
$FLEX_{FC}$ -FLEX	-	-	0.00	0.00

Table 7

Table 7 Element concentration (in wt%) obtained from SEM-EDX analysis of powder and samples in the reference condition (FLEX) and after the firing cycle ($FLEX_{FC}$).

Sample	Al	V	Ti
Powder	6±1	3.3±0.3	91±7
FLEX	6±1	2.5±0.3	92±7
$FLEX_{FC}$	6±1	2.5±0.3	91±7

Table 8

Table 8 Experimental lattice parameters calculated from peak position in the XRD patterns. Last row reports the nominal lattice parameter values from cards of the International Centre for Diffraction Data (ICDD).

Sample	**α-Ti (nm)**	**β-Ti (nm)**
Powder	a = 0.2922 ± 0.0001 c = 0.4659 ± 0.0001	-
FLEX	a = 0.2922 ± 0.0002 c = 0.4658 ± 0.0004	-
$FLEX_{FC}$	a = 0.2930 ± 0.0001 c = 0.4681 ± 0.0003	a = 0.323 ± 0.002
Nominal	a = 0.29505 c = 0.46826 ICDD card n. 44-1294	a = 0.33065 ICDD card n. 44-1288

Table 9

Table 9 Average value and standard deviation from five measurements of element concentration in α-Ti and β-Ti phases obtained by STEM-EDX analysis performed in spot mode on both FLEX and $FLEX_{FC}$ samples. All values are in wt%.

Sample	Ti phase	Al	V	Ti
FLEX	α	6.10±0.03	2.786±0.001	91.12±0.16
$FLEX_{FC}$	α	6.49±0.04	1.95±0.24	91.6±0.3
$FLEX_{FC}$	β	2.77±0.18	20.3±0.5	76.95±0.24